Impact of the cycling temperature on electrode/electrolyte interfaces within Li4Ti5O12 vs LiMn2O4 cells

Nicolas Gauthier, Cecile Courreges, Julien Demeaux, Cécile Tessier, Hervé Martinez

Impact of the cycling temperature on electrode/electrolyte interfaces within $Li_4Ti_5O_{12}$ vs $LiMn_2O_4$ cells

Nicolas Gauthier[1,2], Cécile Courrèges[1,], Julien Demeaux[2],*

Cécile Tessier[2], and Hervé Martinez[1,3,],*

[1]CNRS/Univ. Pau & Pays Adour / E2S UPPA, Institut des Sciences Analytiques et de Physicochimie pour l'Environnement et les Matériaux – UMR 5254, 64000 Pau, France,

[2]SAFT, 111-113 Boulevard Alfred Daney, 33000 Bordeaux, France

[3]Réseau sur le Stockage Electrochimique de l'Energie (RS2E), CNRS FR3459, 33 Rue Saint Leu, 80039 Amiens Cedex, France

Corresponding Author

*Cécile Courrèges cecile.courreges@univ-pau.fr

ABSTRACT

Reliable development of Li-ion Batteries requires a good understanding of the correlation between electrochemical performances and accurate aging interfaces phenomena. The present study focuses on the SEI characterization formed at both electrodes surface in $LiMn_2O_4/Li_4Ti_5O_{12}$ (LMO/LTO) cells, depending on the cycling temperature, which is one of the major stress factors for batteries. LMO/LTO cells were cycled at 25°C, 40°C and 60°C over 100 cycles and the

chemical composition of surface layers was investigated by XPS, SAM and ToF-SIMS at the end of the 100th cycles. LTO electrodes are covered by surface layers since the first cycle (inducing an irreversible capacity loss) and the SEI thickness increases with the cycling temperature; moreover, organic (alkyl-carbonates, polyethylene oxides, oxalates) and inorganic species (LiF and (fluoro)-phosphates) of the solid interphase are present in different proportions depending of the temperature; more fluorophosphates are especially observed at 60°C due to a higher chemical degradation of $LiPF_6$ salt. Finally, small amounts of manganese, heterogeneously spread over the LTO electrode surface, are found at different oxidation states at higher temperatures; for the first time, metallic Mn^0 was detected at the LTO surface after cycling at 60°C which could explain the important capacity loss of the system at this temperature.

KEYWORDS: Li-ion Batteries, SEI, LTO, LMO, Temperature, XPS, SAM, ToF-SIMS

1. INTRODUCTION

Commercial Li-ion batteries (LiBs) based on graphite and $LiCoO_2$ (LCO) have reached their limits regarding cost and safety[1]. Among the different cell chemistries which could overcome these challenges, the $Li_4Ti_5O_{12}$/$LiMn_2O_4$ (LTO/LMO) system represents an attractive option especially for lithium-ion batteries used in Hybrid Electrical Vehicles (HEVs)[2], due to its fast charge capabilities[3]. Indeed, the three dimensional spinel material $LiMn_2O_4$ (LMO) is a promising cobalt-free cathode material which fulfills the criteria of safety, high energy density (due to its high operating voltage at 4.2 V vs. Li/Li^+) and good thermal stability[4]. Temperature is one of the major factor on LIBs aging and a strict temperature control is needed to ensure the commercial development of LIBs in electrical vehicles[5]. Concerning lithium titanate, $Li_4Ti_5O_{12}$, its capacity of 175mAh/g is lower than graphite (372mAh/g) but its stability in cycling as well as in calendar aging[3,6,7] and its high potential

(1.55 V vs. Li/Li^+) avoiding lithium plating and short-circuits, make it a good candidate, which is already used for electric vehicles[8]. In addition, the high redox reversibility of LTO/LMO cells results in significantly lower expansions during charge and discharge compared to graphite-based cells. For instance, Zhan *et al.*[9] have reported a better capacity retention for LMO/LTO cells compared to LMO/graphite ones. The damages on the active particles, induced by these volume changes during cycling, are therefore less important in LTO than in graphite[7,10]. The main drawback of LTO/LMO cells which limits its implementation on the batteries market, is its low energy density. Nevertheless, Majima *et al*.[7] pointed out that LTO based cells, thanks to its smaller expansion factor, would need less packaging than graphite ones. Consequently, if the encapsulation box is included, LMO/LTO cells would have an energy density of 85.5 Wh/kg compared to 94.8 Wh/kg for LMO/graphite ones, which represents only 11% of difference.

Other aging mechanisms could entail capacity fading depending on the intrinsic properties of active materials and their interactions during cycling. For LTO/LMO system, it was proved that manganese (coming from LMO) dissolution in the electrolyte and deposition at the LTO electrode surface, especially at high temperature (over 55°C), significantly affect electrochemical performances of cells[11,12,13]. In addition, different studies have reported the formation of a "Solid Electrolyte Interphase" (SEI) and an important gas release at the LTO electrode surface[14, 15, 16] coming from the degradation of the electrolyte solvents and the lithium salt, which can lead to a rapid loss of capacity[17]. These surface layers (5-10 nm) play a key role in batteries efficiency as they have to ensure the passivation of the electrode surface by reducing parasitic reactions, while maintaining a good diffusion of lithium ions. In previous papers, our group revealed that Mn deposition at the LTO electrode surface induce a destabilization of the SEI which is a clear issue for LTO/LMO cells[18,19]. Although it is well known that the cycling temperature influence the electrochemical performances of batteries[20,21], the impact of high temperatures on the chemical composition of solid interfaces and the manganese dissolution in LTO/LMO cells after long cycling has to be highlighted. Gieu *et al*. have already analyzed LTO interfaces within half cells after the first cycle at high cycling temperatures[22] but the SEI characteristics of LTO electrodes in full cells and after long cycling remained unexplored. The objective of this new paper is to complete the work initiated in our

laboratory, by characterizing the SEI properties as a function of the temperature in LTO/LMO full cells and after long cycling. To do so, electrochemical performances were correlated to surface analyses after 100 cycles at 25°C, 40°C and 60°C using three main techniques: X-ray Photoelectron Spectroscopy (XPS) which quantitatively determines the chemical environments in interfacial layers, Scanning Auger Microscopy (SAM) which allows the acquisition of highly resolved elemental chemical mappings at the electrode surfaces, and Time-of-Flight Secondary Ion Mass Spectrometry (ToF-SIMS) which characterizes the in-depth spatial distribution of organic and inorganic molecular species within the SEI of LTO electrodes by carrying out high resolution depth profiling experiments and 3D image reconstructions.

2. EXPERIMENTAL SECTION

Electrodes formulation. The first step is the preparation of inks which are coated on an aluminum current collector, calendered and then dried (100°C under vacuum for 12h). These inks are obtained by mixing with a T25 digital ULTRA-TURRAX homogenizer (i) 93 wt% of anhydrous active material (LTO or LMO) supplied by SAFT, (ii) 4 wt% of carbon black (CB) as a conductive additive with a specific surface of 65 $m^2.g^{-1}$ (99.8% purity, nanometric particles Super C65 TIMCAL from Alfa Aesar), and (iii) 3 wt% of poly(vinylidene fluoride) (PVdF) as a binder from Solvay (Solef 5130). In order to focus on LTO performances, the electrodes capacity is limited by the LTO negative electrode active mass. The loadings of LTO and LMO electrodes are ≈9.0 mg LTO/cm^2 and ≈17.0 mg LMO/cm^2 respectively, corresponding to a theoretical capacity rate of C^+/C^-≈0.9. Electrodes with 18 mm of diameter are prepared by punching out the ink foil and porosities of ≈45% and ≈40% for LTO and LMO electrodes are respectively obtained by compression. Finally, all electrodes are dried under vacuum at 110°C for at least 12h in an oven (Büchi, Switzerland) and then transferred into an argon-filled glove box (MBraun, Germany) without exposure to ambient atmosphere.

Batteries cycling. Electrodes are integrated in coin cells using 0.25 mL of electrolyte and two separators (Celgard, 20µm thickness) in polypropylene. The liquid electrolyte is a mixture of ethylene carbonate (EC, anhydrous, 99%

purity) and ethylmethyl carbonate (EMC, purity ≥ 98%) (3:7 in volume), containing $LiPF_6$ lithium salt (purity ≥99.99%, 1 $mol.L^{-1}$). Coin cells are assembled in a glove box, under controlled argon atmosphere with low H_2O/O_2 levels (< 2 ppm). Cells are then cycled at 25°C, 40°C or 60°C in a thermostatic oven, under galvanostatic mode at C/10 rate from open circuit voltage with a Biologic MPG2 (Biologic SA, Claix, France) apparatus for the first cycle, and under galvanostatic mode at C/2 rate for 98 cycles. Finally, a last cycle is performed at C/10 rate to restore the capacity loss due to high C-rate cycling. Note that the first cycle is carried out at low rate in order to ensure the formation of a passivating layer at the LTO electrode surface[21]. Full cells cycling experiments are monitored based on the LTO electrode potential, between 1.0 V and 2.1 V. The coin cells are limited in capacity by the LTO electrodes (the capacity matching between positive and negative is 0.9).

Electrochemical impedance spectroscopy (EIS). After cycling, the system is kept at the open-circuit voltage (2.0 V) for 2 hours; then potential-controlled impedance spectra are recorded from 10 kHz to 10 mHz with a perturbation of 10 mV at 25°C (10 points per decade).

Samples cleaning. After EIS measurements, coin cells are opened in a glove box with low H_2O/O_2 levels (< 2 ppm). Both LTO and LMO electrodes are carefully extracted and rinsed with a large excess of dimethyl carbonate in order to remove all traces of electrolyte.

X-ray Photoelectron Spectroscopy (XPS). XPS analyses are carried out with a Thermo Scientific K-Alpha X-ray photoelectron spectrometer using a focused monochromatized Al-Kα radiation ($h\nu$ = 1486.6 eV). To avoid any moisture or air exposure, the samples are transferred using a transfer vessel to the XPS machine, which is directly connected to an argon dry glove box working at low H_2O/O_2 levels (< 4 ppm). Core ionization peaks are recorded with a 20 eV constant pass energy (PE) over an ellipsoidal area of 200×400 μm^2. Data treatment is performed with CasaXPS software. Peak fitting is processed with a non-linear Shirley-type background and mathematical components are obtained by a weighted least-squares calculation method using 30% Lorentzian and

70% Gaussian line shapes except for the manganese spectra. Indeed, Mn 2p spectra fitting and interpretation are complex due to the multiplet splitting arising from the presence of unpaired electrons in its electronic configuration. This induces asymmetric shapes and close binding energies even for different oxidation states. Therefore, the deconvolution strategy was based on the use of the Mn 2p envelopes of reference compounds in which manganese presents only one oxidation state: Mn^{3+} in Mn_2O_3 and Mn^{4+} in Li_2MnO_3, as previously performed by our group[18,23]. The spectral calibration is done based on the CF_2 component (290.7 eV) originated from the PVdF binder in C 1s core peaks. Quantifications are calculated using Scofield's relative sensitivity factors corrected by -0.6 in intensity.

Scanning Electron Microscopy (SEM) and Scanning Auger Microscopy (SAM). For SEM and SAM analysis at high spatial resolution (~10-100 nm), a JEOL JAMP 9500F Auger spectrometer is used. In order to avoid any sample degradation, samples are transferred from the gloves box to the machine using a transfer vessel. SEM images are recorded using an acceleration voltage of 10 kV and a low target current of 5 nA. Scanning Auger acquisitions are carried out in constant analyzer energy mode to define the useful energy width in order to get a significant intensity difference between the Auger transition and the background shape. An "auto probe tracking" correction (which compares SAM and SEM images recorded after each sequence with the initial reference image) is also used to evaluate and compensate any possible drift during acquisition. The software provided by JEOL is used for processing the chemical mappings. The concentration of each element is materialized individually through a scale of colors (ranging from black for no signal to white for the maximum of signal).

Time-of-Flight Secondary Ion Mass Spectrometry (ToF-SIMS). ToF-SIMS analysis are carried out using a TRIFT V nanoToF II (Physical Electronics, Chanhassen (MN), US) equipped with a 30 kV Au-LMIG. The electrode samples are fixed on the sample holder with a metallic mask and transferred from the gloves box to the spectrometer thanks to a transfer vessel to avoid any air exposure. All mass spectra are obtained using the same experimental conditions, which allows to perform semi-quantitative analysis (comparing the intensity ratios of

peaks). For surface analysis, the LMIG gun is tuned to deliver Au_3^{++} primary ions with a direct current (DC) of 12 nA over a 50 µm raster size and the number of frames is set to 30 (dose: $2.2x10^{12}$ ions/cm^2) over 0 – 400 mass range for both polarities. Depth profile experiments (series of 30 "analysis/sputtering" cycles) are carried out using the previous conditions for surface analysis (Au^+, 50x50µm^2 raster size) and a 3 kV Ar^+ gas gun for etching (with an etching time of 20 seconds for each cycle, a DC current of 150 nA and a sputtered area of 500x500 µm^2). Note that $^6Li^+$ and $^7Li^+$ peaks in positive polarity and $^{19}F^-$ and $^{16}O^-$ peaks in negative polarity appear very intense and have to be blanked during the measurement in order to detect better smaller peaks. Data processing is performed using ToF-DR software provided by PHI company. All negative polarity spectra are calibrated using OH^- (m/z 17), C_2H^- (m/z 25) and LiF_2^- (m/z 45) peaks and all positive polarity mass spectra are calibrated using K^+ (m/z 39), Li_2F^+(m/z 33) and Ti^+(m/z 48) peaks. For depth-profiles graphical representation, the intensity of the secondary ions of interest was normalized related to the total ion counts for both polarities.

3. RESULTS AND DICUSSION

3.1 Electrochemical results

Galvanostatic profiles of LMO/LTO cells at 25°C (in blue), 40°C (in green) and 60°C (in red) for the 1st cycle, 99th cycle and 100th cycle are presented in Figure 1a, Figure 1b and Figure 1c, respectively. After the first charge, LTO capacities at 25°C (173 mAh.g^{-1}) and 40°C (172 mAh.g^{-1}) are close to the theoretical value (175 mAh.g^{-1}) whereas the capacity is a bit higher at 60°C (178mAh.g^{-1}). Moreover, after the first discharge, capacity losses of 4 mAh.g^{-1}, 8 mAh.g^{-1} and 19 mAh.g^{-1} are measured at 25°C, 40°C and 60°C respectively, which indicates that Li^+ ions (supplied by positive electrodes in excess) are irreversibly consumed by parasitic reactions to form surface layers; this phenomenon appears to be more important at 60°C compared to 40°C and 25°C. After the 99th charge at C/2 (figure 1b), capacities decrease for all temperatures compared to the first charge, especially at 60°C. This observation indicates a decrease of both reversible and irreversible capacities upon cycling. Moreover, capacity values are the same after the 99th discharge than after the 99th charge, which evidences a stabilization of the capacity after cycling. A higher C-rate regime induces an accumulation of lithium ions at

intercalation sites[4]. When the charge is carried out more quickly, some sites will not have the time to be fully occupied by lithium ions, which causes a loss of capacity and a higher polarization of the system. At 40°C and 60°C, the electrons and Li^+ ions mobility is more limited than at 25°C probably due to the formation of thicker layers at the electrodes surface. The last 100th cycle is performed at a lower c-rate C/10 (figure 1c) in order to completely discharge the accumulator. Capacities of 8 mAh.g^{-1} at 40°C and 19 mAh.g^{-1} at 60°C are restored between charge and discharge, whereas at 25°C there is no difference between the two states of charge of the cell; moreover, the capacity after the 100th cycle at 25°C reaches 172 mAh.g^{-1} which is in agreement with a small polarization and a weak fading of the system at this temperature. On the contrary, at 60°C, the polarization remains higher due to an important loss of capacity during cycling, which limits the performance of cells.

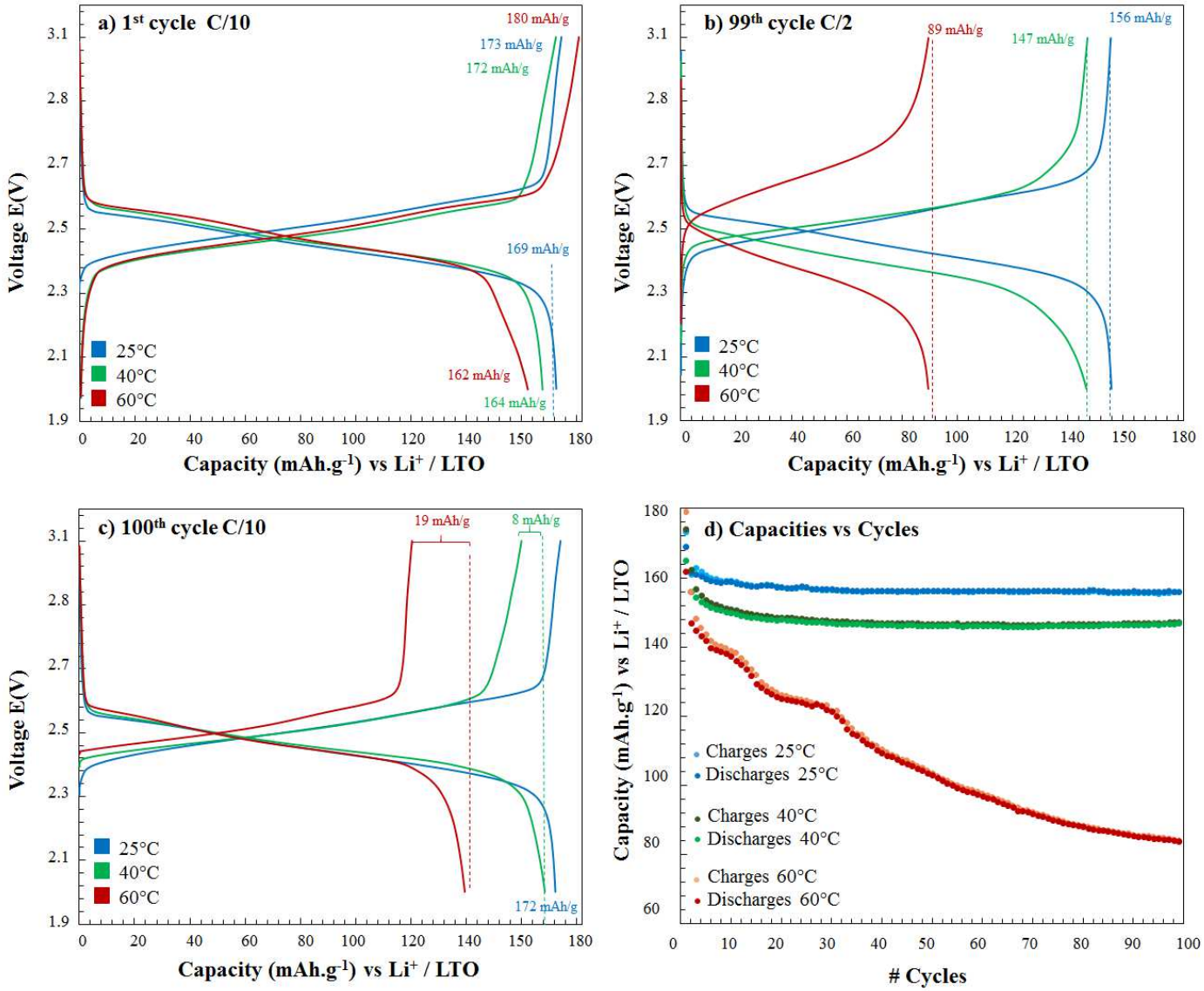

Figure 1. Galvanostatic charge/discharge voltage profiles of LTO/LMO cells at 25°C (in blue), 40°C (in green) and 60°C (in red) a) for the 1st cycle at C/10, b) for the 99th cycle at C/2 and c) for the 100th cycle at C/10 ; Charge and discharge capacities of LMO/LTO systems cycled at 25°C (in blue), 40°C (in green) and 60°C (in red) for the first 100 cycles d). (in color)

Figure 1d shows the evolution of charge and discharge capacities as a function of the cycle number for LMO/LTO coin cells at 25°C (in blue), 40°C (in green) and 60°C (in red) and confirms the previous observations. A fastest degradation rate appears at 60°C whereas no obvious capacity fading appears for LMO/LTO cycled at 25°C. Indeed, the capacity retention becomes stable after five cycles for 25°C, whereas it is after 30 cycles for 40°C and no stability in capacity is obtained for 60°C (the coulombic efficiency is under 99.8%). Consequently, the degradation of cells increases with the temperature, in accordance with growth of impedance system. The Nyquist impedance curves of LMO/LTO full cells after 100 cycles at 25°C (in blue), at 40°C (in green) and at 60°C (in red) are shown in Figure S1. An equivalent circuit (inset in figure S1) is used for fitting the electrodes behavior, in which R_s, R_f, and R_ct correspond to the ohmic resistance, the film resistance, and the charge transfer resistance, respectively. Constant phase elements CPE_f and CPE_{dl} are used to replace the film capacitance (C_f) and the double-layer capacitance (C_{dl}). The coefficient a_f relates to the roughness of the electrodes surface[17]. The fitted parameters are summarized in Table S1. The film resistance increases with the cycling temperature, which may imply a greater accumulation of insoluble compounds. A gradual decrease of a_f is observed with higher temperature. This might imply that the interfacial film covering electrodes surface at 40°C and 60°C may be less uniform than the ones formed at 25°C.

To further investigate the correlation between electrochemical performances and the cycling temperature, XPS, SAM and ToF-SIMS surface analysis techniques were used to characterize the chemical composition of surface layers formed on both LTO and LMO electrodes.

3.2 Surface analysis

3.2.1 Reversibility of the redox process: *XPS analysis*

Figure 2 presents XPS Ti 2p core peaks of the pristine LTO negative electrode (first line) and LTO electrodes after 100 cycles at 25°C (second line), 40°C (third line) and 60°C (fourth line) versus LMO electrodes (column a) and Mn 2p core peaks of the pristine LMO positive electrode (first line) and LMO electrodes after 100 cycles at 25°C (second line), 40°C (third line) and 60°C (fourth line) versus LTO electrodes (column b). Note that the LTO lithiation (charge of the battery) corresponds to a reduction process of titanium ($Ti^{4+} \rightarrow Ti^{3+}$) and to an oxidation of manganese ($Mn^{3+} \rightarrow Mn^{4+}$).

At the pristine electrodes surface, Ti and Mn 2p signals are split into two components ($2p_{3/2}$ and $2p_{1/2}$) due to spin-orbit coupling. Ti 2p spectra consist of a Ti $2p_{3/2}$ component at 458.7 eV and Ti $2p_{1/2}$ one at 464.4 eV, in agreement with Ti^{4+} ions in an oxygen environment. Concerning Mn 2p spectra, the envelope maxima for each component-doublet, located at 641.4 eV and 642.2 eV, are respectively attributed to Mn^{3+} (from Mn_2O_3 reference) and Mn^{4+} (from Li_2MnO_3 reference) type ions of the $LiMn_2O_4$ material.

After cycling, the two components of Ti^{3+} signal (Ti $2p_{3/2}$ and Ti $2p_{1/2}$ at 456.8 eV and at 458.4 eV respectively), related to the lithiation/reduction process of LTO, are still detected and their proportion increase with the temperature (Ti^{3+} signal represents 25% of the total detected titanium at 60°C, 20% at 40°C and 7% at 25°C). This is attributed to the irreversible consumption of Li^+ ions and/or to the slower electrons and ions transportations onto LTO electrodes due to the formation of a thicker interfacial film at higher temperature. Indeed, Ti 2p is less detected at the LTO electrode surface after cycling at 40°C (3.6 at. %) and 60°C (1.2 at. %) compared to 25°C (4.5 at. %). At the end of the hundredth discharge (100 cycles), the Mn 2p spectra are very similar to the one of the pristine electrode for all cycling temperatures, which shows the good reversibility of the electron transfer over cycling at the LMO electrode. The overall quantity of detected manganese at the LMO electrode surface decreases in the same proportion for the three temperatures compared to the pristine one (from 4.6 at. % to ~3.0 at. %), which also suggests a covering of LMO electrodes by a surface layer. All these observations are in agreement with an increase of the capacity loss with high temperature.

Note that the titanium and manganese are detected after cycling at all the temperatures which indicates that the thickness of the interfacial layers are lower than 10 nm for both systems, as the XPS analysis depth is about 5-10 nm.

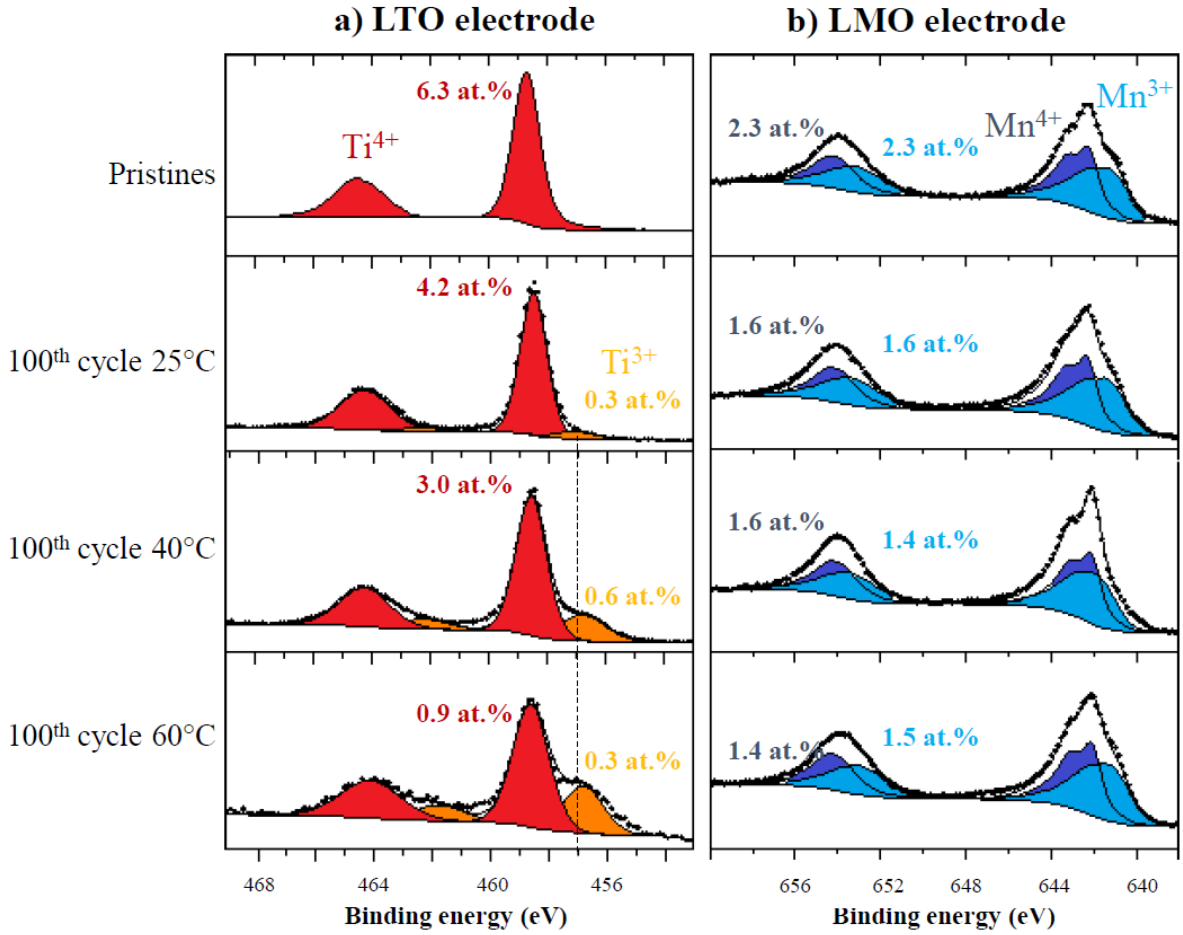

Figure 2. a) Ti 2p XPS spectra of the pristine LTO negative electrode (first line) and LTO electrodes after 100 cycles at 25°C (second line), 40°C (third line) and 60°C (fourth line) and b) Mn 2p core peaks of the pristine LMO positive electrode (first line) and LMO electrodes after 100 cycles at 25°C (second line), 40°C (third line) and 60°C (fourth line). (in color)

3.2.2 Characterization of the chemical composition of surface layers: *XPS analysis*

Figure 3 presents XPS O 1s (a) and F 1s (b) core peaks of the pristine LTO negative electrode (first line) and LTO electrodes after 100 cycles at 25°C (second line), 40°C (third line) and 60°C (fourth line) versus LMO

electrodes. O 1s and F 1s core peaks of the pristine LMO positive electrode and LMO electrodes are shown in supporting information (figure S2).

XPS O 1s spectrum of LTO pristine electrode shows a narrow peak at 530.1 eV which is characteristic of O^{2-} anions of the LTO crystalline network. The two other minor peaks at higher binding energy are assigned to weakly absorbed species at the electrode surface (**O**–H or **O**=C and C–**O**–C chemical environments) and represent 2.3 at. % of the total surface species. After cycling, new O 1s components appear at 531.5 eV and 532.5 eV attributed to oxygenated species deposited at the electrode surface such as polyethylene oxides or $ROCO_2Li$, which are the main components of electrolyte solvent decomposition, and at 533.5 eV which is assigned to (fluoro)phosphates ((PO_4^{3-}), $PO(RO)_3$ or $Li_XPO_yF_z$), resulting from the decomposition of $LiPF_6$ salts and reactions with solvent degradation products[24]. At the same time, the LTO O 1s component strongly decreases at high temperature; it counts only for 2.7 at. % at 60°C compared to 9.2 at. % at 25°C. This evidences the covering process during cycling of LTO electrodes by a surface layers whose thickness increase with the temperature. In agreement with O 1s spectra, the appearance of new C 1s components after cycling on C 1s spectra (data not shown) at 286.7 eV, 287.8 eV and 289.5 eV, attributed to C-O, C=O and **O**=C-O/CO_3^{2-} chemical environments respectively, confirms the deposition of organic species at the LTO electrodes surface, which is more important at high temperature.

Concerning F 1s spectrum for the LTO pristine electrode, the two PVdF components, attributed to C**F**$_2$ and C**F**$_3$ / C**F**$_2$-**C**F$_2$ environments, are observed at 687.9 eV and 689.5 eV respectively. After cycling, the PVdF CF_2 component decreases when the temperature increases which proves once again the formation of a thicker surface layer at the LTO electrode surface at high temperature; on the contrary, the intensity of C**F**$_3$ / C**F**$_2$-**C**F$_2$ component slightly increases with the temperature due to probable degradation and rearrangement of PVdF. Moreover, two new F 1s components are detected after cycling at 685.0 eV (light gray) which corresponds to LiF and at 686.5 eV (dark gray) attributed to fluorophosphates ($Li_xPO_yF_z$). The proportion of these last one increases with the temperature (2.0 at. % at 25°C, 4.1 at. % at 40°C and 8.7 at.% at 60°C), whereas no major difference is observed

at low and high temperatures for the LiF component. These results confirm a chemical degradation process of $LiPF_6$ salt more important at high temperature.

For LMO electrodes (figure S2), the proportion of surface species also increases with the temperature but in lesser extent. A greater proportion of fluorophosphates is detected at the LMO electrodes surface after cycling, whatever the temperature, which may be due to the cycling at high voltage (4.15V) on the positive electrode side in agreement with the literature[19,24,25]. This result suggests that a dissolution process of fluorophosphates at the LMO electrode surface and their deposition at the LTO electrode surface after migration through the electrolyte, may occur and this phenomenon is more important at high temperature. In the same way, organic species formed at the LMO electrode (by oxidation of the solvents) can also migrate to the LTO electrode which can explain their greater accumulation at high temperature at the negative electrode surface. Indeed, the important decomposition of $LiPF_6$ salt at high temperature could entail a change in the $LiPF_6$ dissociation equilibrium in LiF and PF_5 (as a strong Lewis acid) which catalyzes the solvents degradation in the electrolyte, especially EC[26,27,28].

P 2p core peak (data not shown) also exhibits an increase of phosphates/fluorophosphates proportions at the LTO electrodes surface when the cycling temperature increases from 25°C to 60°C and to a lesser extent at LMO electrodes surface too, which is consistent with the previous observations. Note that fluorophosphates could come from parasitic reactions between POF_3 (formed by PF_5 decomposition at high temperature) and solvents of the electrolyte, which leads to gaseous releases and severe fading[29].

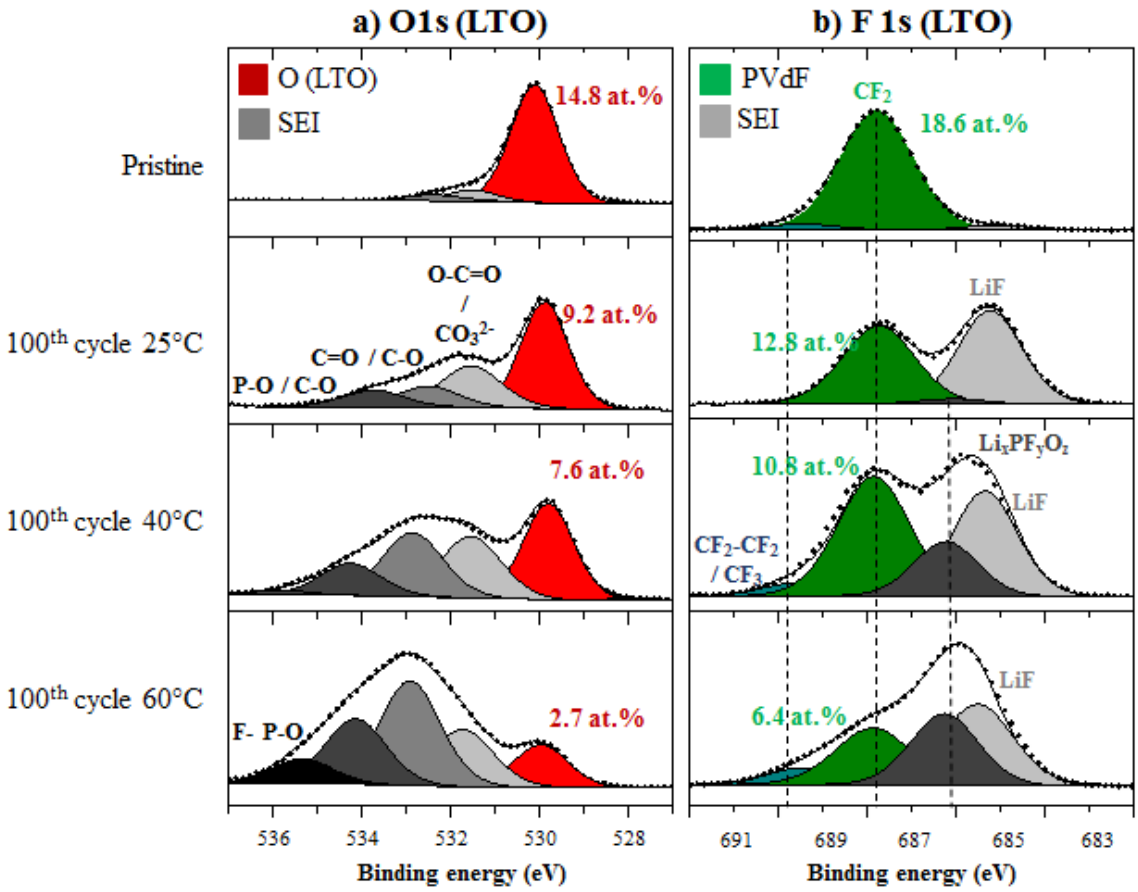

Figure 3. a) O 1s and b) F 1s XPS spectra of the pristine LTO negative electrode (first line) and LTO electrodes after 100 cycles at 25°C (second line), 40°C (third line) and 60°C (fourth line) versus LMO electrodes. (in color)

The quantitative analysis from O 1s, C 1s, F 1s, Li 1s and P 2p core peak is presented in figure 4a and 4b for LTO and LMO electrodes respectively. The atomic percentages of LTO electrode (in red), LMO one (in blue) and deposited surface species (in grey) during cycling are reported in figure 4. Note that to determine the atomic percentages of electrodes, the proportions of active materials, carbon black and PVdF components were added; similarly, the amount of surface species corresponds to the sum of organic and inorganic species proportions calculated from XPS spectra. As mentioned before, both LTO and LMO electrodes are covered by surface layers after cycling at 25°C, 40°C and 60°C. The SEI thickness formed at LTO electrodes increases with the temperature, especially at 60°C, whereas the temperature influence is less noticeable for LMO surface layers; these ones are slightly thicker at 60°C, which could be in agreement with the capacity and impedance evolution upon cycling,

but to a lesser extent compared to LTO electrode. In all cases, surface layers remain thinner than the XPS depth of analysis (~10 nm) as the electrode components are still detected.

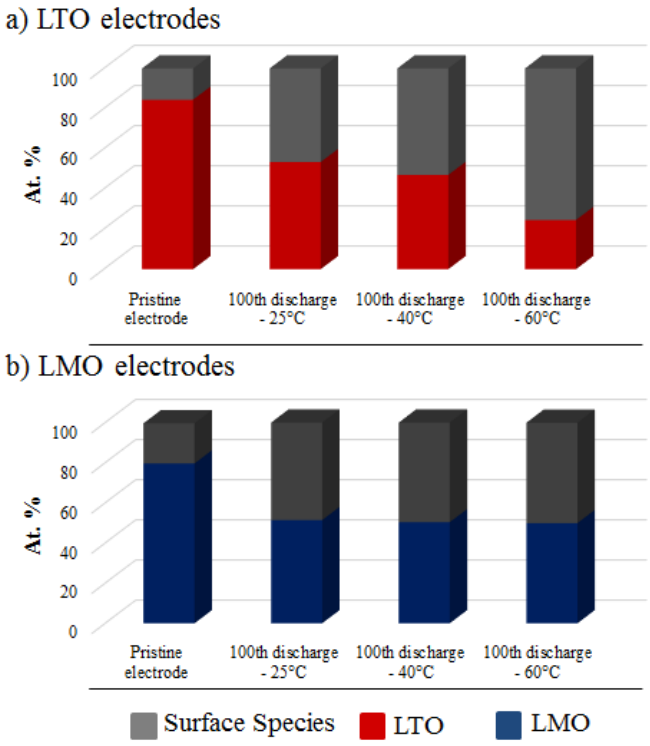

Figure 4. Histograms comparing the atomic percentages of surface species (in grey), LTO electrode components (in red), LMO electrode components (in blue) detected at the surface of LTO electrodes a) and LMO electrodes b) before cycling (pristine electrode) and after 100 cycles at 25°C, 40°C and 60°C. (in color)

Manganese is detected by XPS (figure 5) at the LTO electrode surface cycled versus LMO after the 100th charge and 100th discharge at 40°C and 60°C but not at 25°C. This manganese, which comes from a dissolution of the LMO active material at the positive electrode, migrates through the electrolyte and is deposited at the negative electrode surface over cycling. Mn 2p spectra at 40°C display a maximum of intensity between 641.3 eV and 642.0 eV with satellites characteristic of manganese in the oxidation state +II[30]. According to Gieu *et al.* and Kim *et al.*[18,31] this manganese is originated from MnF_2 and MnO compounds, which could induce the increase of cells impedance. At 60°C, the amount of detected manganese at the LTO electrode surface is more important

and a new peak appears at 638.0 eV which is attributed to metallic manganese Mn^0. The $LiPF_6$ decomposition more pronounced at high temperature could lead to an acidification of the electrolyte (HF formation) which promotes the manganese dissolution of LMO spinel and may induce its reduction until the metallic state[9,32]. These manganese species can favor the re-oxidation/reduction of certain SEI species and the release of lithium ions, leading to a delay in the SEI stabilization[11,31,33,34,35]. Thus, in the case of LTO/LMO cycled at high temperatures, other mechanisms than the electrochemical reduction of solvents at the LTO electrode surface have to be considered to explain the formation of the SEI layer. On one hand, deposited species come from the dissolution of the positive electrode and migration through the electrolyte (like manganese species and fluorophosphates) and on the other hand, a catalytic phenomenon, increasing the electrolyte degradation due to the presence of manganese species, can occur at the interface. Thereby, the formation of MnO and MnF_2 at the LTO electrode surface could come from the reaction between the electrolyte and deposited manganese species.

Inductively-coupled plasma (ICP) measurements were performed on LTO/LMO full cells cycled at 60°C which allow to determine a manganese concentration of around 40 ppm in the electrolyte. This value may be underestimated because some of the dissolved Mn species are deposited on the electrodes surface. Nevertheless, the LMO active material loss caused by dissolution in the electrolyte is not substantial. Besides, as the operating voltage of LMO (at 4.15 V vs. Li^+/Li) is much higher than the reduction potential of manganese ions, these ones can only be deposited on LTO anodes and have no significant influence on LMO cathodes. Therefore, the increase of cells resistance is mainly attributed to changes on the LTO anodes side.

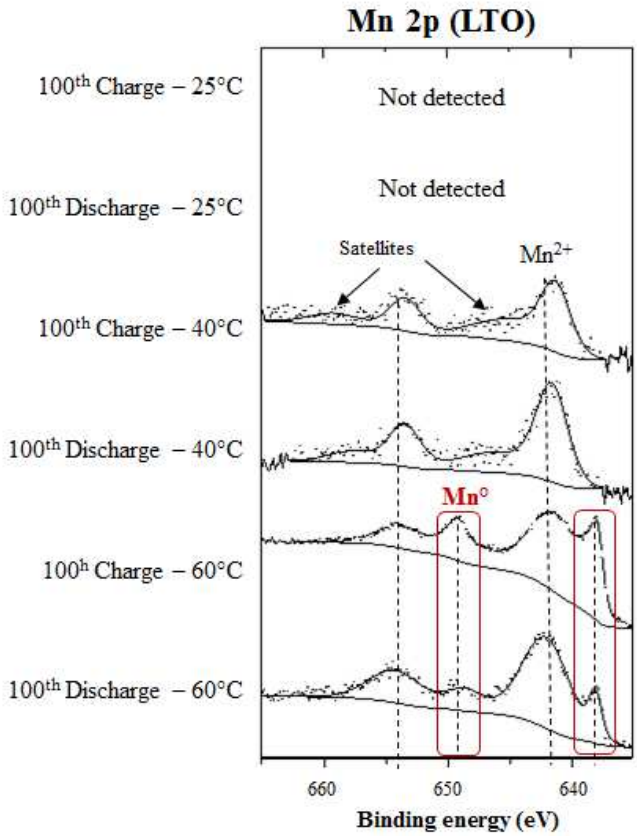

Figure 5. Mn 2p XPS spectra of cycled LTO electrodes versus LMO after the 100th charge and after the 100th discharge at 25°C, 40°C and 60°C. (in color)

3.2.4 Spatial distribution of elemental chemical species at LTO electrodes surface: *SAM analysis*

SEM images and SAM mappings of LTO electrodes surface after 100 cycles at 25°C a), 40°C b) and 60°C c) are presented in Figure 6. Two different types of particles are distinguishable on the SEM picture: the ones attributed to LTO grains in light grey, and the ones corresponding to the carbon black in dark grey. After cycling, the deposition and growing of the SEI with the temperature cannot be demonstrated by SEM as the obtained images are similar to the pristine electrode one (figure S3). On SAM images, the overlap of titanium and oxygen mappings (figure S3) confirm the localization of LTO particles for all the temperatures. Nevertheless, at 40°C and 60°C, oxygen and carbon are detected besides the LTO and carbon black particles which proves one more time the deposition of organic species on the LTO electrode surface, due to the SEI formation, whose thickness increases at high temperature. However, Titanium is still detected at the end of the hundredth discharge at 60°C,

which means that the SEI is thinner than 5 nm. The phosphorus mappings reveal the presence of fluorophosphates mainly localized on LTO particles especially at 40°C and 60°C, which highlights a preferential reactivity of the lithium salt anion with the active material[19]. Concerning fluorine compounds, a more homogeneous repartition is revealed on LTO electrode cycled at 40°C compared to electrodes cycled at 25°C (for which fluorine species are mainly located on black carbon) and at 60°C (for which fluorine species are preferentially deposited on LTO particles). According to XPS analysis at 25°C, SEI fluorine species are mainly originated from LiF, which is preferentially located on the carbon black[22]. At higher temperatures, and especially at 60°C, fluorine signal is generated by LiF but also by fluorophosphates which are present in greater quantity; these results are in agreement with the mass spectrometry measurements performed by Gachot *et al*[27]. Finally, despite the detection of manganese by XPS at 40°C and 60°C, SAM manganese mapping is only obtained at 60°C and indicates a heterogeneous distribution over the LTO electrode surface as previously suggested by Börner *et al*.[21].

The SEI layer formed at the LMO positive electrode/electrolyte interface was also analyzed by SAM after cycling but the mappings are not presented here for a non-exhaustive presentation. Note that fluorophosphates are preferentially deposited on the LMO active material particles but no difference is noticeable with the temperature increase.

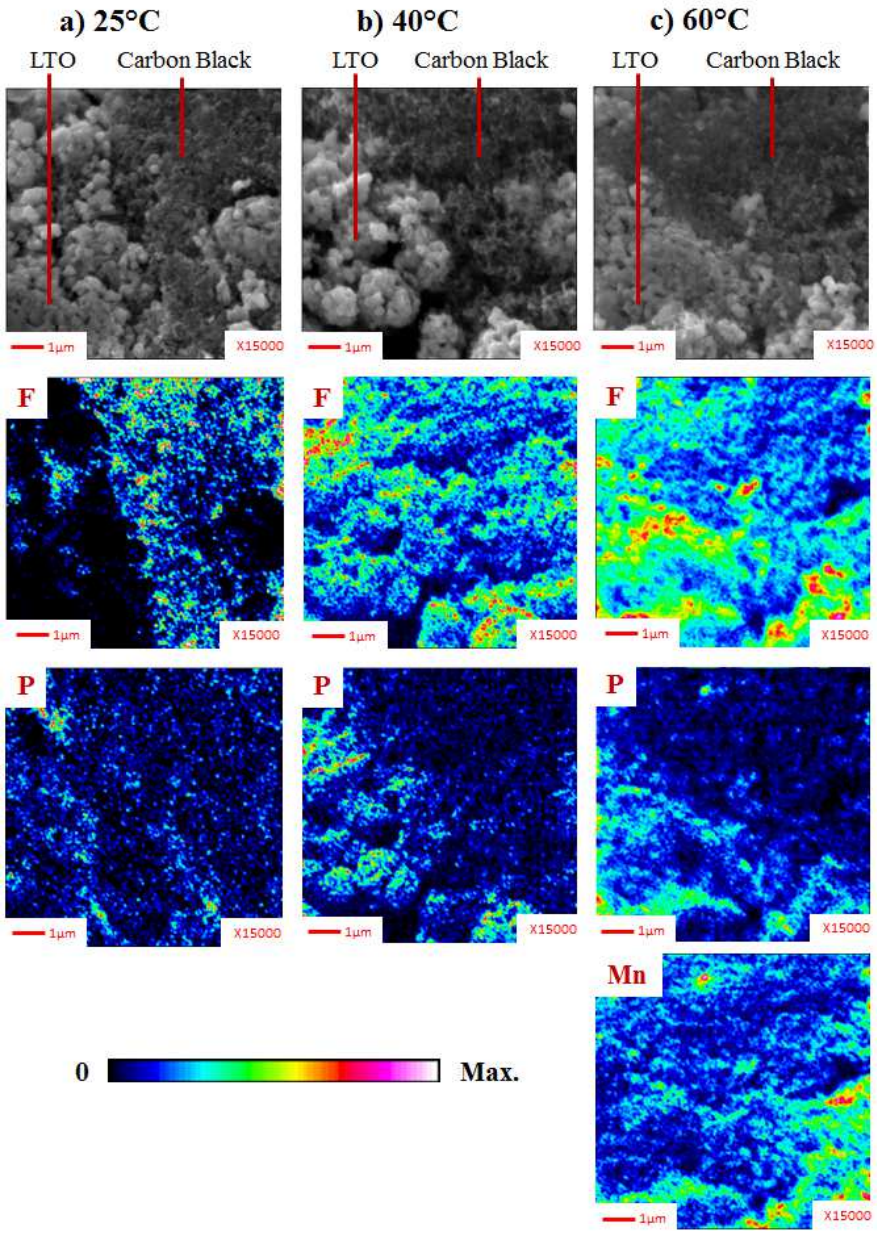

Figure 6. SEM images and SAM chemical mappings of fluorine F, phosphorus P and manganese Mn on LTO electrodes surface at the end of the hundredth discharge for LTO/LMO cells cycled at 25°C a), 40°C b) and 60°C c). (in color)

3.2.5 In depth distribution of organic and inorganic molecular species at LTO electrodes surface: *ToF-SIMS analysis*

Figure 7 shows the mass spectra in negative polarity of cycled LTO negative electrodes at the end of the hundredth cycle at 25°C a), 40°C b) and 60°C c) over 0-120 m/z range. At the end of the hundredth cycle, the main negative secondary ions detected are carbonaceous species like m/z: 12 (C^-), m/z: 13 (CH^-), m/z: 24 (C_2^-), m/z: 25 (C_2H^-) related to solvents degradation, and fluorine and phosphorus containing species m/z: 45 (LiF_2^-), m/z: 63 (PO_2^-), m/z: 79 (PO_3^-) and m/z: 101 ($PO_2F_2^-$), characteristics of the SEI formation from $LiPF_6$ salt decomposition[36]. The most intense peak m/z: 17 (OH^-) come from solvent degradation but also from the LTO active material. At 40°C and 60°C, the intensity of peaks attributed to phosphate species is higher than at 25°C, suggesting that the SEI at the LTO electrode cycled at higher temperature is thicker due to more important salt degradation, which is consistent with our previous XPS results. The mass spectra in positive polarity are shown in supporting information (figure S4).

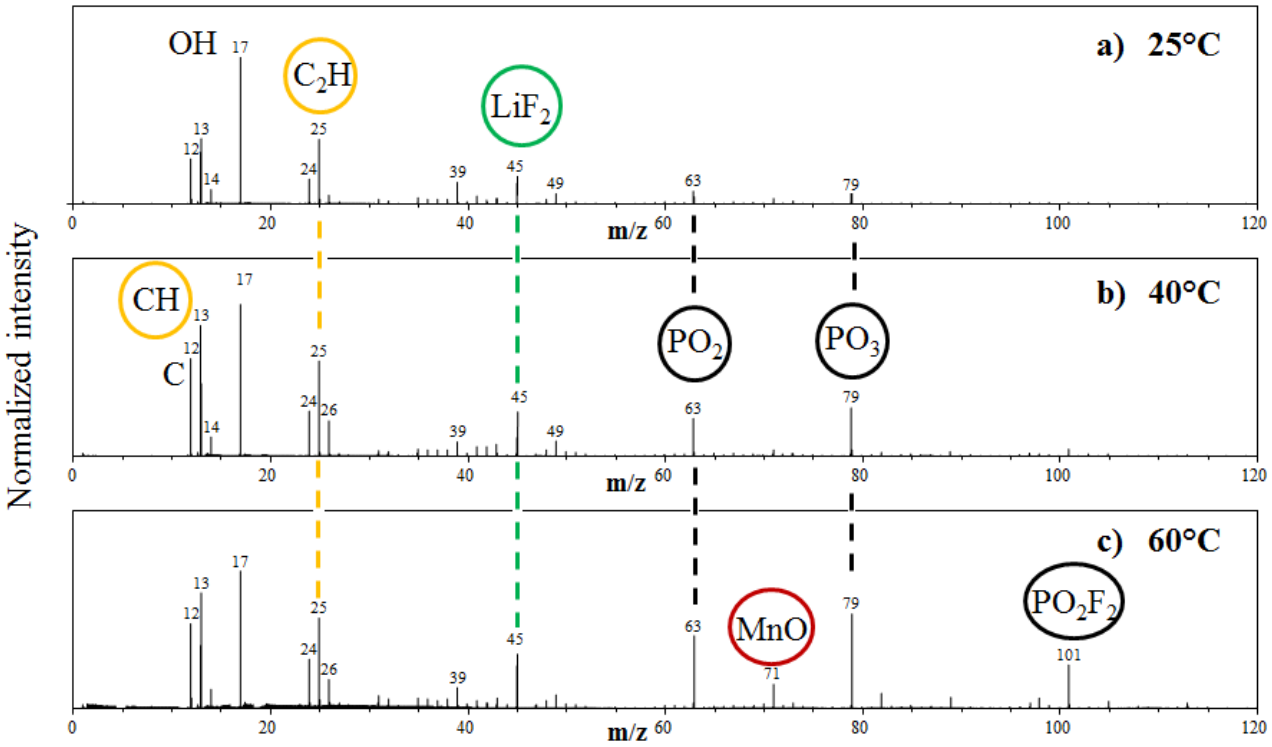

Figure 7. ToF-SIMS negative ion spectra over a 0-120 m/z range for LTO electrodes cycled at 25°C a), 40°C b), and 60°C c) at the end of the hundredth cycle. (in color)

Moreover, m/z: 71 (MnO^-) secondary ions (as well as m/z: 55 (Mn^+) in positive polarity, data not shown), specific of the LMO active material, are detected at the LTO electrode surface cycled at 60°C[18,31], which confirms the dissolution process of the LMO electrode and manganese deposition at the LTO electrode surface at high cycling temperature.

In order to have more information about Manganese and SEI species in-depth spatial distribution at the LTO electrode surfaces, depth-profiles experiments (series of "analysis/sputtering" cycles) were performed in positive and negative polarities after the hundredth cycles at 25°C a), 40°C b) and 60°C. Figure 8 presents the normalized TOF-SIMS depth profiles obtained for Ti^+ (representing the LTO active material, blue line), Li_2F^+ (characteristic of inorganic SEI species, green line), MnO^- (coming from LMO dissolution, red line), $C_3H_6O^+$ (specific of organic SEI species, yellow line) and PO_2^- (arising from $LiPF_6$ salt decomposition, black line) secondary ions of interest over 400 seconds of etching depending on the cycling temperature.

A distinct rise of the bulk active material species (Ti^+) intensity is observed during etching for all temperatures, but the slope of the curve is more important at lower temperature (0.8 normalized intensity is reached after 150 second for 25°C, after 200 seconds for 40°C and after 275 seconds for 60°C), which clearly evidences the increase of the SEI thickness with higher temperatures. At 25°C, $C_3H_6O^+$ and PO_2^- normalized intensities decreases quickly to reach almost zero after the first sputtering phase (30 seconds) while Li_2F^- signal intensity, initially higher, increases, which proves that organic and phosphate species are mainly located at the extreme surface of the SEI and above Li_2F species. The proportion of these last ones gradually decreases during the remaining sputtering time, which evidences that Li_2F compounds are present more deeply into the SEI. At 40°C, $C_3H_6O^+$, PO_2^- signals follow the same trend as at 25°C by decreasing mainly during the first sputtering cycle, but the proportion of PO_2^- remains slightly higher over a longer etching time than at 25°C, meaning their proportion increases a little bit at 40°C. This time, no initial increase of Li_2F^- intensity is observed during the first sputtering phase which shows that organic, phosphate and LiF species are mixed together at the extreme surface of the SEI. At 60°C, $C_3H_6O^+$, PO_2^- and Li_2F^- secondary ions are present in higher proportion at the beginning of

the etching compared to 25°C and 40°C, which is consistent with a more important salt decomposition at 60°C, as previously highlighted by SAM and XPS. Like at lower temperatures, $C_3H_6O^+$ and PO_2^- signal intensities mainly decrease during the first sputtering phases at 60°C, which means they are located in majority at the SEI extreme surface, but the intensities remain higher over a longer etching time compared to 40°C, meaning they are present in higher proportions and more deeply into the SEI. Concerning Li_2F^-, its proportion gradually decreases from the beginning of the sputtering (corresponding to the SEI top surface) to the end of the etching (related to the inner of the SEI). Finally, concerning manganese related species, the MnO^- normalized intensity is much higher at 60°C than at 40°C (for which the signal has been increased x15 for a better visibility), which is again consistent with a dissolution of LMO, migration through the electrolyte and deposition at the LTO electrode surface more important at 60°C. The normalized intensity of MnO^- increases after the first sputtering phase and decreases gradually during the remaining sputtering time, which evidences that manganese species are covered by organic and inorganics species at the extreme surface and are present deeply into the SEI.

To better visualize the spatial in-depth distribution of the considered species, 3D images have been reconstructed from depth-profile experiments and are presented under each graph related to one temperature. The signal intensity of Ti^+(in blue), Li_2F^+ (in green), $C_3H_6O^+$ (in yellow) and PO_2^- (in black) secondary ions is plotted over the analyzed area (50µm x 50µm = x and y dimensions) versus the etching time (the z axis, 400s, which is over dimensioned compared to the other axes) for the three temperatures. When a color is not appearing anymore on the image, it means the signal intensity of the secondary ion is too low in the mass spectrum to be considered. For 60°C, another 3D image, representing the spatial in-depth distribution of MnO^- (in red) and Ti^+ (in blue) secondary ions, is presented separately for better clarity. Note that the intensity of MnO^- at 40°C is too weak to be imaged in 3D.

The 3D map at 25°C clearly highlights that organic and phosphate compounds are located only at the extreme surface of the SEI and that they cover LiF species which insert more deeply into the SEI. The same behavior is observed at 40°C except that LiF species are also present at the extreme surface and phosphate species proportion is slightly higher. At 60°C, the increase of the SEI thickness is clearly visible on the 3D map, where

all species are present in higher proportions. The same trend as at lower temperature is obtained, where organic and phosphate species are mainly located in the upper part of the SEI while LiF compounds are continuously present from the top surface to the inner part of the SEI. The manganese species 3D map clearly evidences their presence within the SEI and their covering by the upper part of the SEI (composed of inorganics, organics and phosphate species). All these results are consistent with our previous XPS and SAM results[18,19,37] and the literature[27,28,36] and confirm that both salt decomposition (inducing an important LiF and phosphate species deposition at the LTO electrode) and manganese dissolution are intensified at high temperature, which explains lower electrochemical performances of LTO/LMO cells at 60°C.

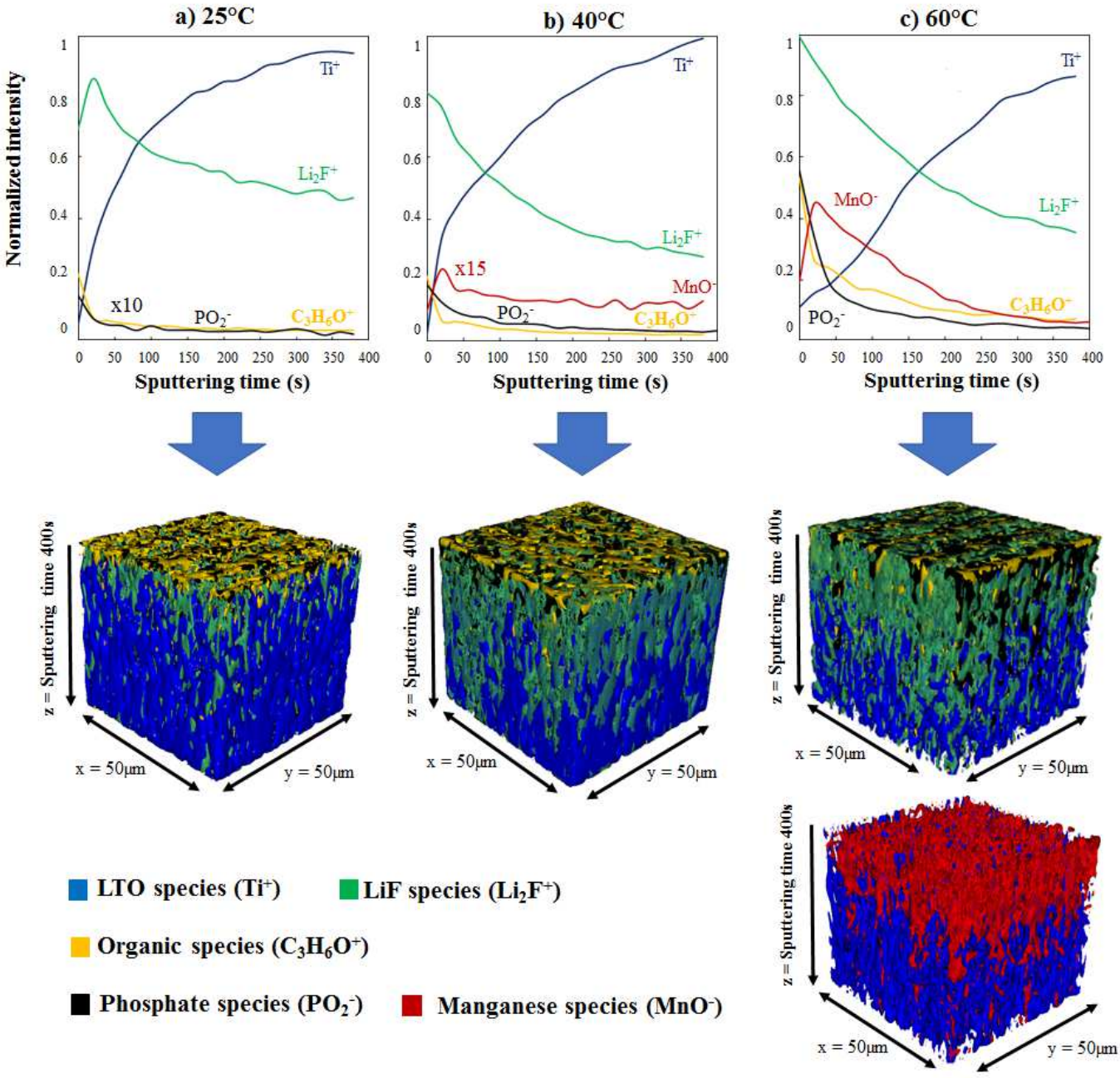

Figure 8. Normalized ToF-SIMS depth profiles over 400 s of Ti^+, Li_2F^+, $C_3H_6O^+$, PO_2^- and MnO^- secondary ions detected at the LTO electrode surface cycled facing LMO after the hundredth cycle at 25°C a), 40°C b) and 60°C c). 3D image reconstructions related to each depth profile, representing the in-depth spatial distribution of LTO (in blue), organic (in yellow), LiF (in green) and phosphates (in black) species. For better clarity, the 3D map representing manganese species (in red) with LTO (in blue) at 60°C is presented separately. (in color)

4. CONCLUSIONS

In conclusion, this work contributes to a better understanding of the impact of the temperature on LTO electrode/electrolyte interfaces in LTO/LMO systems. Thanks to the complementarity of XPS, SAM and ToF-SIMS techniques, it was clearly proved that high temperatures (60°C) increase the SEI thickness and change its chemical composition as well as the in-depth spatial distribution of SEI species. Indeed, the important $LiPF_6$ salt decomposition at 60°C induces the formation and deposition at LTO surface of (fluoro)phosphate species in higher proportions, as well as a more important manganese dissolution at the LMO positive electrode, which migrates through the electrolyte and insert within the SEI; moreover, metallic manganese was detected for the first time by XPS at the LTO electrode surface, which could be linked to the PF_5 degradation mechanism at the electrode/electrolyte interface. All these factors destabilize the SEI formed at the LTO electrode surface and can cause the loss of capacity of LTO/LMO cells at high temperature.

Such manganese dissolution detrimental effect will have to be controlled to allow the commercialization of LTO-based LIBs composed of lithium manganese oxides or derivatives. Several options need to be investigated to minimize the fading of LTO/LMO cells at high temperature, like the use of additives in the electrolyte or the replacement of $LiPF_6$ by fluorophosphates free salts; the coating or doping of lithium titanate particles could also be of interest. Moreover, as the NMC electrode presents less active materials dissolution during cycling and better electrochemical performances than LMO when cycled facing LTO[19], a blend of NMC and LMO materials could be considered as a good option for the positive electrode.

ACKNOWLEDGEMENTS

The authors gratefully acknowledge SAFT company, the French CNRS (national center for scientific research) and The French National Research Agency via the project ANR-11-EQPX-0027 MARSS for financial support.

REFERENCES

[1] Etacheri, V.; Marom, R.; Elazari, R.; Salitra, G.; Aurbach, D. Challenges in the development of advanced Li-ion batteries: a review. *Energy Environ. Sci.*, 4, 3243 (2011).

[2] Yi, T.-F.; Jiang, L.-J.; Shu, J.; Yue, C.-B.; Zhu, R.-S.; Qiao, H.-B. Recent development and application of $Li_4Ti_5O_{12}$ as anode material of lithium ion battery. *J. Phys. Chem. Sol.* 71 (2010) 1236.

[3] Takami, N.; Inagaki, H.; Tatebayashi, Y.; Saruwatari, H.; Honda, K.; Egusa, S. High-power and long-life lithium-ion batteries using lithium titanium oxide anode for automotive and stationary power applications, *Journal of Power Sources*, vol. 244, pp. 469 – 475, 2013.

[4] M. M. Thackeray. Structural considerations of layered and spinel lithiated oxides for lithium ion batteries. *Journal of The Electrochemical Society*, 142(8): 2558–2563, 1995.

[5] Bandhauer, T. M.; Garimella, S.; Fuller, T. F. A critical review of thermal issues in lithium-ion batteries. *Journal of The Electrochemical Society,* 2011, *158*, R1.

[6] Yuan, T.; Tan, Z.; Ma, C.; Yang, J, Ma, Z. -F.; Zheng, S. Challenges of spinel $Li_4Ti_5O_{12}$ for lithium-ion battery industrial applications. *Adv Energy Mater* (2017).

[7] Majima, M.; Ujiie, S.; Yagasaki, E.; Koyama, K.; Inazawa, S. Development of long life lithium ion battery for power storage, *Journal of Power Sources*, vol. 101, no. 1, pp. 53 – 59, 2001.

[8] Pistoia, G. Lithium-ion batteries: advances and applications. *Elsevier*, 2014.

[9] Zhan, C.; Lu, J.; Kropf, J.; Wu, T.; Jansen, A. N.; Sun, Y.-K.; Qiu, X.; Amine, K. Mn(II) Deposition on Anodes and its Effects on Capacity Fade in Spinel Lithium Manganate–Carbon Systems. *Nature Communications* 2013, 4, 2437.

[10] Ohzuku, T. Zero-strain insertion material of $Li[Li_{1/3}Ti_{5/3}]O_4$ for rechargeable lithium cells. *Journal of the Electrochemical Society* **1995**, 142, no. 5: 1431–35.

[11] Vetter, J.; Novák, P.; Wagner, M.; Veit, C.; Möller, K.-C.; Besenhard, J.; Winter, M.; Wohlfahrt-Mehrens, M.; Vogler, C.; Hammouche, A. Ageing mechanisms in lithium-ion batteries, *Journal of Power Sources*, vol. 147, no. 1 - 2, pp. 269 – 281, 2005.

[12] Wohlfahrt-Mehrens, M.; Vogler, C.; Garche, J. Aging mechanisms of lithium cathode materials, *Journal of Power Sources*, vol. 127, no. 1-2, pp. 58 – 64, 2004.

[13] Choi, N.-S.; Yeon, J.-T.; Lee, Y.-W.; Han, J.-G.; Lee, K.T.; Kim, S.-S. Degradation of spinel lithium manganese oxides by low oxidation durability of $LiPF_6$-based electrolyte at 60 °C Solid State Ionics, 219 (2012) 41-48.

[14] Song, M.-S.; Kim, R.-H.; Baek, S.-W.; Lee, K.-S.; Park, K.; Benayad, A. Is $Li_4Ti_5O_{12}$ a Solid-Electrolyte-Interphase-Free Electrode Material in Li-ion Batterie? Reactivity between the $Li_4Ti_5O_{12}$ Electrode and Electrolyte, *Journal of Materials Chemistry A* 2014, 2 (3), 631-636.

[15] He, Y.-B.; Li, B.; Liu, M.; Zhang, C.; Lv, W.; Yang, C.; Li, J.; Du, H.; Zhang, B.; Yang, Q.-H.; Kim, J.-K.; Kang, F. Gassing in $Li_4Ti_5O_{12}$-based Batteries and its Remedy, *Scientific Reports* 2 2012.

[16] Gieu, J. -B.; Courrèges, C.; El Ouatani, L.; Tessier, C.; Martinez, H. Influence of Vinylene Carbonate Additive on the $Li_4Ti_5O_{12}$ Electrode/electrolyte Interface for Lithium-ion Batteries. *Journal of the Electrochemical Society* 2013, 164(6) A1314-A1320.

[17] Wu, K.; Qian, L.; Sun, X.; Wu, N.; Zhao, H.; Zhang, Y. Influence of manganese ions dissolved from $LiMn_2O_4$ cathode on the degradation of $Li_4Ti_5O_{12}$-based lithium-ion batteries. *J Solid State Electrochem*. (2017).

[18] Gieu, J.-B.; Winkler, V.; Courrèges, C.; El Ouatani, L.; Tessier, C.; Martinez, H. New Insights in the Characterization of the Electrode/electrolyte interfaces within $LiMn_2O_4/Li_4Ti_5O_{12}$ cells, by X-ray Photoelectron Spectroscopy, Scanning Auger Microscopy and Time-of-Flight Secondary Ions Mass Spectrometry. *Journal of material Chemistry* A 2017, 5, 15315-15325.

[19] Gauthier, N.; Courrèges, C.; Goubault, L.; Demeaux, J.; Tessier, C.; Martinez, H. Influence of the Positive Electrode on $Li_4Ti_5O_{12}$ (LTO) Electrode/Electrolyte Interfaces in Li-Ion Batteries. *Journal of the Electrochemical Society* (**2018**), 165 (13) A2925-A2934.

[20] Wright, D. R.; Garcia-Araez, N.; Owen, J. R. Review on high temperature secondary Li-ion batteries. *Energy Procedia* 151 (2018) 174-181.

[21] Börner, M.; Klamor, S.; Hoffmann, B.; Schroeder, M.; Nowak, S.; Würsig, A.; Winter, M.; Schappacher, F. M. Investigations on the C-Rate and Temperature Dependence of Manganese Dissolution/Deposition in $LiMn_2O_4/Li_4Ti_5O_{12}$ Lithium Ion Batteries. *Journal of the Electrochemical Society*, 163(6): A831–A837, 2016.

[22] Gieu, J.-B.; Courrèges, C.; El Ouatani, L.; Tessier, C.; Martinez, H. Temperature Effects on $Li_4Ti_5O_{12}$ Electrode/electrolyte interfaces at the first cycle: A X-ray Photoelectron Spectroscopy and Scanning Auger Microscopy Study. *Journal of Power Sources* 2016, 318, 291–301.

[23] Grissa, R.; Martinez, H.; Cotte, S.; Galipaud, J.; Pecquenard, B.; Le Cras, F. Thorough XPS analyses on overlithiated manganese spinel cycled around the 3V plateau. Applied Surface Science 411 (2017) 449–456.

[24] Wu, K.; Qian, L.; Sun, X.; Wu, N.; Zhao, H.; Zhang, Y. Influence of manganese ions dissolved from $LiMn_2O_4$ cathode on the degradation of $Li_4Ti_5O_{12}$-based lithium-ion batteries. *Solid State Electrochem.* DOI 10.1007/s10008-017-3773-2

[25] Yan, P.; Zheng, J.; Kuppan, S.; Li, Q.; Lv, D.; Xiao, J.; Chen, G.; Zhang, J. -G.; Wang, C. -M. Phosphorus Enrichment as a New Composition in the Solid Electrolyte Interphase of High Voltage Cathodes and Its Effects on Battery Cycling. *Chem. Mater.*, october 2015.

[26] Campion, C. L.; Li, W.; Lucht, B. L. Thermal Decomposition of $LiPF_6$-Based Electrolytes for Lithium-Ion Batteries. *Journal of the Electrochemical Society,* 152 (12) A2327-A2334 (2005).

[27] Gachot, G.; Grugeon, S.; Armand, M.; Pilard, S.; Guenot, P.; Tarascon, J.-M.; Laruelle, S. Deciphering the multi-step degradation mechanisms of carbonate-based electrolyte in Li batteries. *Journal of Power Sources*, 178 (2008) 409-421.

[28] Parimalam, B. S.; MacIntosh, A. D.; Kadam, R.; Lucht, B. L. Decomposition Reactions of Anode Solid Electrolyte Interphase (SEI) Components with $LiPF_6$. *J. Phys. Chem. C* 2017, 121, 22733-22738.

[29] Kraft, V.; Weber, W.; Grutzke, M.; Winter, M.; Nowak, S. Study of decomposition products by gas chromatography-mass spectrometry and ion chromatography-electrospray ionization-mass spectrometry in thermally decomposed lithium hexafluorophosphate-based lithium ion battery electrolytes. *RSC Advances*, 5, 80150 (2015)

[30] Biesinger, M. C.; Payne, B. P.; Grosvenor, A. P.; Lau, L. W.; Gerson, A. R.; Smart, R. S. Resolving Surface Chemical States in XPS Analysis of first Row Transition Metals, Oxides and Hydroxides: Cr, Mn, Fe, Co and Ni. *Applied Surface Science* 2011, 257, 2717–2730.

[31] Kim, D.; Park, S.; Chae, O. B.; Ryu, J. H.; Kim, Y. -U.; Yin, R. -Z.; Oh, S. M. Re-Deposition of Manganese Species on Spinel LiMn2O4 Electrode after Mn Dissolution. *Journal of the Electrochemical Society*, 159 (3) A193-A197 (2012)

[32] Gao, Y.; Dahn, J. Correlation between the growth of the 3.3 V discharge plateau and capacity fading in Li1+xMn2-xO4 materials, *Solid State Ionics*, vol. 84, no. 1–2, pp. 33 – 40, 1996.

[33] Lee, Y. K.; Park, J.; Lu, W. A Comprehensive Study of Manganese Deposition and Side Reactions in Li-Ion Battery Electrodes. *Journal of the Electrochemical Society*, 164 (12) A2812-A2822 (2017).

[34] Aoshima, T.; Okahara, K.; Kiyohara, C.; Shizuka, K. Mechanisms of manganese spinels dissolution and capacity fade at high temperature. *J. Power Sources* 97–98 (2001) 377.

[35] Gilbert, J.A.; Shkrob, I. A.; Abraham, D. P. Transition Metal Dissolution, Ion Migration, Electrocatalytic Reduction and Capacity Loss in Lithium-Ion Full Cells. *Journal of The Electrochemical Society*, 164 (2) A389-A399 (2017).

[36] Li, W.; Dolocan, A.; Oh, P.; Celio, H.; Park, S.; Cho, J.; Manthiram, A. Dynamic behaviour of interphases and its implication on high-energy-density cathode materials in lithium-ion batteries. *Nature Communications*, 8:14589 (2017).

[37] Gauthier, N.; Courreges, C.; Demeaux, J.; Tessier, C.; Martinez, H. Probing the in-depth distribution of organic/inorganic molecular species within the SEI of LTO/NMC and LTO/LMO batteries: A complementary ToF-SIMS and XPS study. *Applied Surface Science*, 2020, 501, 144266.

Supporting Information:

Impact of the temperature on electrode/electrolyte interfaces within $Li_4Ti_5O_{12}$ vs $LiMn_2O_4$ cells

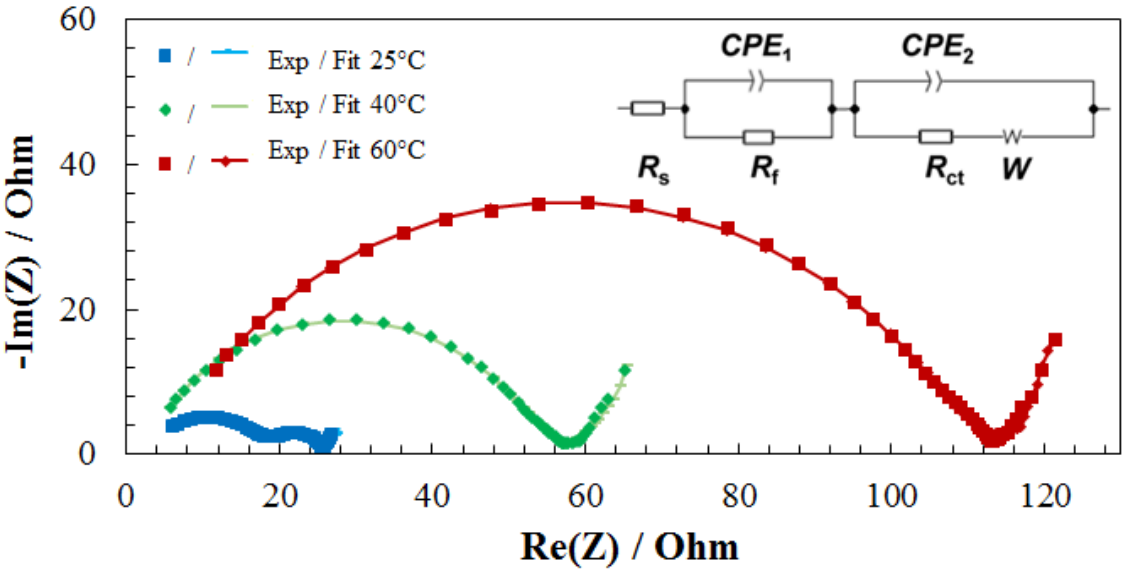

Figure S1. Experimental (Exp) Electrochemical Impedance Spectroscopy results of LMO/LTO full cells at 25°C and fitted curves (Fit) at 0% SOC, after 100 cycles operating at 25°C (in blue), 40°C (in green) and 60 °C (in red) (the circuit used to fit the electrodes behavior is shown). (in color)

Table S1. The fitted EIS data of LMO/LTO full cells cycled at 25°C, 40°C and 60°C

Temperature	**Re (Ohm)**	**CPE_1**		**Rf / Ohm**	**CPE_2**		**Rct / Ohm**	**W**
		Q_f (10^{-6})	**a_f**		**Q_{dl} (10^{-3})**	**a_{dl}**		
25°C	2.1	82.8	0.8	17.4	2.0	0.9	5.1	2.2
40°C	2.7	30.0	0.8	50.4	6.6	0.7	4.3	2.1
60°C	5.0	18.3	0.7	104.3	17.2	0.6	5.4	2.0

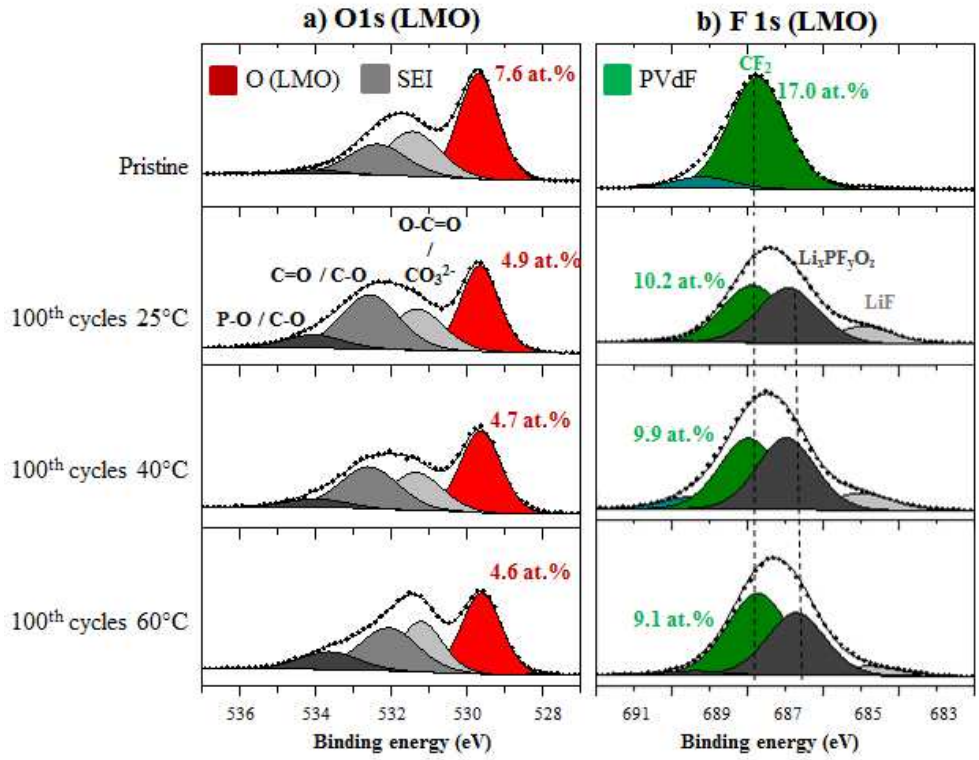

Figure S2. a) O 1s and b) F 1s XPS spectra of the pristine LMO positive electrode (first line) and the LMO electrodes after 100 cycles at 25°C (second line), 40°C (third line) and 60°C (fourth line) versus LTO electrodes. (in color)

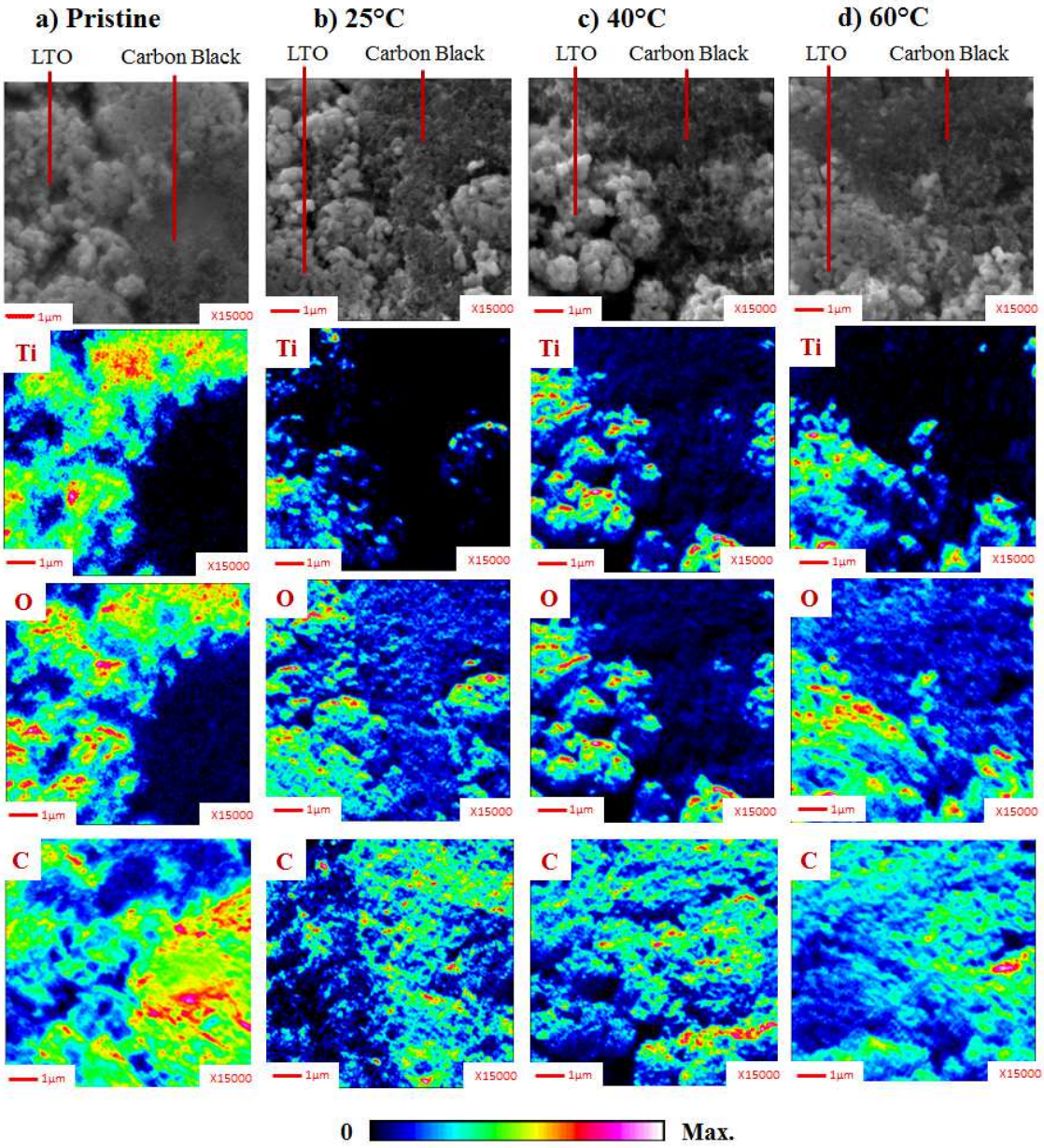

Figure S3. SEM images and SAM chemical mappings of titanium Ti, oxygen O, and carbon C on LTO electrodes surface for the pristine electrode a), at the end of the hundredth discharge for LTO/LMO cells cycled at 25°C b), 40°C c) and 60°C d). (in color)

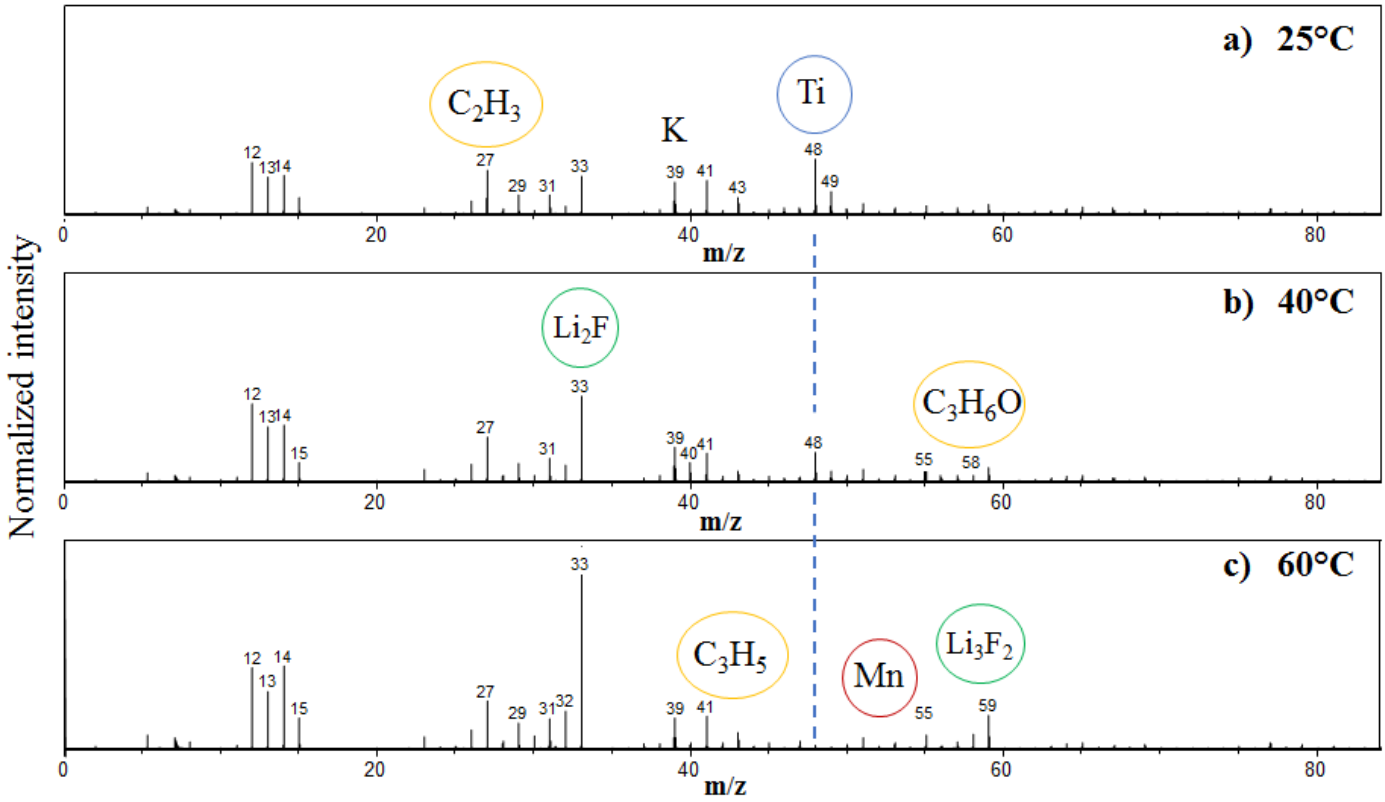

Figure S4. ToF-SIMS positive ion spectra over a 0-90 m/z range for LTO electrodes cycled at 25°C a), 40°C b), and 60°C c) at the end of the hundredth cycle. (in color)